High Performance 3D Si/Ge Nanorods Array Anode Buffered by TiN/Ti Interlayer for Sodium-Ion Batteries

Chuang Yue, Yingjian Yu, Shibo Sun, Xu He, Binbin Chen, Wei Lin, Binbin Xu, Mingsen Zheng, Suntao Wu, Jing Li, Junyong Kang, and Liwei Lin*

3D micro/nanobatteries in high energy and power densities are drawing more and more interest due to the urgent demand of them in integrating with numerous micro/nanoscale electronic devices, such as smart dust, miniaturized sensors, actuators, BioMEMS chips, and so on. In this study, the electrochemical performances of 3D hexagonal match-like Si/Ge nanorod (NR) arrays buffered by TiN/Ti interlayer, which are fabricated on Si substrates by a cost-effective, wafer scale, and Si-compatible process are demonstrated and systematically investigated as the anode in sodium-ion batteries. The optimized Si/TiN/Ti/Ge composite NR array anode displays superior areal/specific capacities and cycling stability by reason of their favorable 3D nanostructures and the effective conductive layers of TiN/Ti thin films. Sodium-ion insertion behaviors are experimentally investigated in postmorphologies and elemental information of the cycled composite anode, and theoretically studied by the first principles calculation upon the adsorption and diffusion energies of sodium in Ge unit cell. The preferential diffusion of sodium in Ge structure over in Si lattice is evidently proved. The successful configuration of these distinctive wafer-scale Si-based Na-ion micro/nanobattery anodes can provide insight into exploring and designing new Si/Ge-based electrode materials, which can be integrated into micro-electronic devices as on chip power systems in the future.

1. Introduction

Rapid development of the integrated circuit (IC) and micro/nanoelectro mechanical system (M/NEMS) technologies are promoting the continued emergence or commercialization of the miniaturized autonomous devices such as wireless sensor networks in smart grid.[1–4] In order to operate independently, the micro/nanoautonomous electronic devices must have on-board power supply. The combination of energy harvesting system from ambient sources (solar, thermal, and vibrational) with a rechargeable battery has been proposed to create a completely self-sustaining power system.[5,6] However, the battery miniaturization still cannot keep pace with the size scaling-down of the complementary metal-oxide semiconductor (CMOS) electronic technologies, due to the poor electrochemical performance of the micro/nanobatteries or the incompatible battery fabrication process with the IC technologies. Currently, the transition from 2D to 3D rechargeable lithium-ion batteries (LIBs) with better electrochemical properties in a small areal footprint was found to cope well with state-of-the-art semiconductor technologies conceptually providing new opportunities for micro/nanopower systems in the future.[7–9]

Very recently, as an alternative energy storage technology to LIBs, the sodium-ion battery (SIB) drew significant attention due to its unlimited sodium sources, low cost (about \$150 ton^{-1} for sodium carbonate versus \$5000 ton^{-1} for lithium carbonate[10] and the higher value of the Na/Na^+ potential (–2.7 V versus standard hydrogen electrode (SHE)) compared to Li/Li^+ (–3.0 V versus SHE), which can effectively reduce the electrolyte degradation at the surface of the electrode material.[11,12] But the major obstacle for the wide spread use of Na-ion batteries at room temperature is the larger ionic radius of Na^+ (0.98 Å) than that of Li^+ (0.69 Å), which makes them more difficult to reversibly insert into and extract from host materials.[11,13] Within the survey of the existing numerous electrode materials for LIBs, only a few cathode candidates borrowed or guided by the Li-ion chemistry are suitable to allow Na ions inserting/deinserting reversibly, and moreover, the availability of such anode host materials is even more rare.[14–17] Excitingly, the theoretical calculations predicted that the sodium could alloy with germanium (Ge) to form NaGe ($Ge + Na^+ + e^- \leftrightarrow NaGe$), giving a theoretical capacity of 369 mAh g^{-1}.[18]

C. Yue, Y. Yu, S. Sun, X. He, W. Lin, Prof. S. Wu, Prof. J. Li, Prof. J. Kang
Department of Physics/Pen-Tung Sah Institute of Micro-Nano Science and Technology
Xiamen University
Xiamen, Fujian 361005, China
E-mail: lijing@xmu.edu.cn
C. Yue, Prof. J. Li, Prof. L. Lin
Department of Mechanical Engineering
University of California
Berkeley, California 94720, USA
B. Chen, B. Xu, Dr. M. Zheng
State Key Lab of Physical Chemistry of Solid Surfaces and Department of Chemistry
College of Chemistry and Chemical Engineering
Xiamen University
Xiamen, Fujian 361005, China

DOI: 10.1002/adfm.201403648

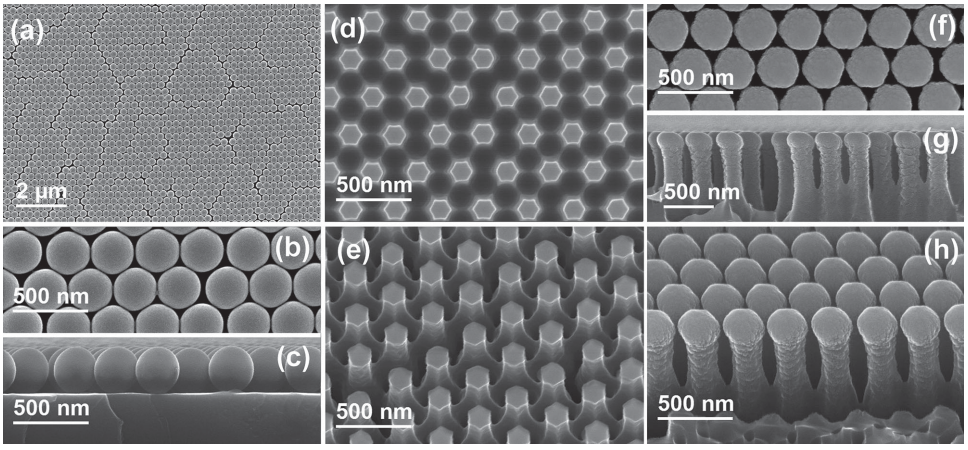

Figure 1. a–c) SEM images of the Si substrate coated by the monolayer PS nanosphere template; d) planar; and e) tilt views of the Si NR arrays produced by the ICP etching using the corresponding PS nanosphere template of (c); f) top; g) section; and h) tilt views of the Si/TiN/Ti/Ge NR arrays after the consecutive sputtering processes.

Additionally, the electrochemical properties of dense and nanocolumnar Ge thin films synthesized by glancing angle deposition technique were investigated showing the promise for Ge as a potential anode materials for SIBs.[19] Recently, Farbod et al. employed the cosputtering technique to fabricate the Tin–Germanium–Antimony alloy thin film anodes applied in SIBs also maintaining an appreciable electrochemical performance.[20] Also, the recently published work experimentally demonstrated that the improved electrochemical performances can be achieved in the Li-activated Ge nanowires or thin film due to the amorphization of the active materials to facilitate the nucleation of Na_xGe.[21] But to date, few studies of the Na-ion reactions with Si and Ge, especially applied in the wafer scale 3D Na-ion micro/nanobatteries presenting excellent cycle performances have been reported.

In this work, the 3D hexagonal match-like Si/TiN/Ti/Ge nanorod (NR) arrays, firstly initiated as anodes in SIBs, were fabricated by nanosphere lithography, inductive coupled plasma (ICP) dry etching, and then followed sputtering techniques. This novel Si/Ge core/shell NR arrays with an interlayer of TiN/Ti thin film display high reversible areal/specific capacity and superior cycling stability due to their firmly and orderly anchoring on Si substrates in 3D configuration, Ge's amorphous nature and improved electronic conductivity, which are beneficial for tackling the drawbacks of large volume expansion and improving the Na-ion kinetics during Na-ion ingress/egress processes. Different postwashing procedures in cycled Ge-composited 3D Si/TiN/Ti NR anodes were experimentally carried out to help investigate the sodium insertion-related electrochemical process. Furthermore, the favorable Na-ion adsorption and diffusion behaviors in Ge electrode materials versus Si were also evidenced via first principles calculations. This unique wafer-scale 3D Si/Ge composite micro/nanoSIB electrodes portend a promising future for their practical applications as a milli/microwatts power supply in M/NEMS or other smart electronic systems.

2. Results and Discussions

2.1. Morphologies and Structures

Figure 1a–c shows the scanning electron microscopy (SEM) images of the as-fabricated 2D PS nanosphere template with the sphere diameter of about 300 nm hexagonally arranged on silicon substrate. As displayed in Figure 1d–e, 3D Si NR arrays were produced with the NRs' size of about 140 nm in the top by the ICP etching using corresponding PS nanosphere template shown in Figure 1c as the mask. It is obvious that the 3D Si NR arrays exhibit the hexagonal topography and good uniformity in distribution and size. The subsequent sheath of TiN/Ti/Ge thin films coating on the patterned Si substrate were constructed by sputtering technique as shown in Figure 1f–h. Compared with the only Si NR arrays in Figure 1d, the space between the Si/TiN/Ti/Ge NRs is narrowed and the hexagonal match-like morphology is presented in the NRs with a height of about 700 nm.

The energy-dispersive X-ray spectrometer (EDS) characterization result shown in **Figure 2**a reveals that TiN/Ti and Ge

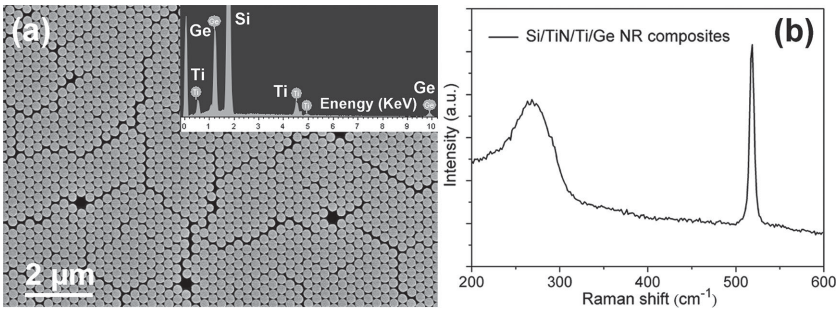

Figure 2. a) SEM image of Si/TiN/Ti/Ge NR arrays in a large area with the corresponding EDS pattern in the inset; b) Raman spectrum of the Si/TiN/Ti/Ge composite NRs.

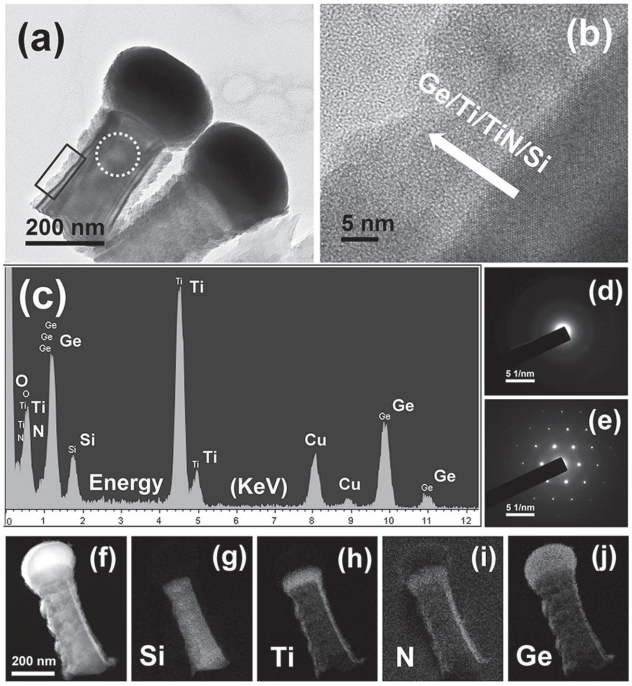

Figure 3. a) TEM image of the Si/TiN/Ti/Ge composite NRs; b–d) HRTEM image, EDS, and SAED patterns taken from the marked area (rectangle) in (a); e) SAED pattern corresponding to the area outlined by the dash ring in (a); f) Dark-field TEM image and g–j) corresponding EDS element mappings of Si, Ti, N, and Ge in another individual Si/TiN/Ti/Ge composite NR.

contents are successfully deposited on the 3D hexagonal Si NR arrays. The reason for the absence of the N element can be attributed to the light element itself. As the layout in Figure 2b, the nature of Ge layer in the Si/TiN/Ti/Ge nanocomposite was also verified by Raman spectra, in which the Raman shift located at about 280 cm^{-1} can be corresponding to the amorphous Ge material.[22]

Transmission electron microscopy (TEM) images and the corresponding selective area electron diffraction (SAED) patterns as displayed in **Figure 3** further evidenced the morphologies and crystal structures of the as-prepared Si/TiN/Ti/Ge composites. Two adjacent Si/TiN/Ti/Ge composite NRs as seen in Figure 3a exhibits a good verticality along the whole length and display the match-like structure, and the surface of each single Si NR presents homogeneous sheath coverage. Figure 3b–d layout the high resolution TEM (HRTEM) image, EDS, and SAED patterns all taken from the marked area (rectangle) in Figure 3a. As seen in the high magnification image of Figure 3b, the Si core and the TiN/Ti/Ge shell layers are all in close contact with a whole thickness of about 30 nm in the shell layers. No lattice fringes were characterized in the outermost Ge shell area indicating the majorly amorphous nature of the as-deposited Ge material. This is also confirmed by SAED pattern as shown in Figure 3d, where both diffraction spots and circles are absent. The EDS pattern in Figure 3c once again verify the existence of corresponding Ge, Ti, and N elements in the as-prepared Si/TiN/Ti/Ge NR, which is consistent with above characterization results. Figure 3e shows the SAED pattern taken from the marked area (dash ring) in Figure 3a that clearly indicates the single crystallinity of the Si core. Dark-field TEM image of another individual match-like Si/TiN/Ti/Ge composite NR and the corresponding element mappings are displayed in Figure 3f–j. The TiN/Ti interlayer is obviously located between the Si core and the outermost Ge sheath layer. Just, a spreading contour displays in the N elemental mapping result, which is understandably caused by the light element itself and the N_2 residue around the sample since N_2 gas is generally used to vent the TEM high vacuum chamber. The corresponding EDS line scans across the Si/TiN/Ti/Ge NR were carried out as shown in Figure S1 (Supporting Information), which show the consistent elemental information with above results and further demonstrate the consecutive sputtering characteristic. The thickness of the TiN/Ti and Ge thin film layers on the "match-stick" surface can be estimated to be about 15–20 and 10–15 nm, respectively. Meanwhile, on the "match-head" part, the thickness of the above two layers are about 60 and 100 nm, respectively.

2.2. Electrochemical Properties

Figure 4a shows cyclic voltammetry (CV) profiles of the Si/TiN/Ti/Ge composite NR anode at a scan rate of 0.5 mV s^{-1} between 0.001 and 1.5 V versus Na/Na^+ from the cycle 1 to 10. In the sodiation branch of all cycles, the characterized reduction peak at about 10–350 mV can be attributed to the reaction of Na ions inserting into the Ge material, while during the opposite desodiation process, a broad peak observed at 600–900 mV is proposed to be corresponding to the Na–Ge dealloying process. This is the up-to-date first report about the CV characteristics of the Na ions inserting/deinserting from the 3D pure amorphous Ge electrode nanomaterials without any preactivation process.[21] After first 5 cycles, the following CV curves almost overlap with each other, which implies good Na-ion insertion/extraction stability in the amorphous Ge anode nanomaterials in SIBs.

As shown in Figure 4b, the cycling performances of 3D Si/TiN/Ti/Ge composite NR anode were measured in the potential range of 0.001–1.5 V versus Na/Na^+ under the constant current density of 10 μA cm^{-2} by comparing with those in 3D Si/Ge NR, 3D Si NR, and planar Si/TiN/Ti/Ge composite electrodes. Apparently, the 3D Si/TiN/Ti/Ge composite NR electrode exhibits the best electrochemical performances among all the fabricated samples possessing and maintaining a reversible areal capacity of about 20 μAh cm^{-2} even after 200 cycles, while the 3D Si/Ge NR, 3D Si NR, and planar Si/TiN/Ti/Ge composite electrodes dramatically dropped in the capacities and terminated their operations after 15 cycles. It should be noticed that in the 3D Si/TiN/Ti/Ge anode, there are the discharge capacity decay and low initial coulombic efficiencies (CE: defined by the charge capacity divided by the discharge capacity) during the first 10 cycles, which might be ascribed to the electrolyte decomposition, irreversible reactions, and slow activation effects. Afterward, the corresponding areal capacity maintained at a steady values of about 20 μAh cm^{-2} due to the cease of the side reactions and the stabilization effect.

Considering the only difference of TiN/Ti layers between the 3D Si/TiN/Ti/Ge composite and Si/Ge NR electrodes and much

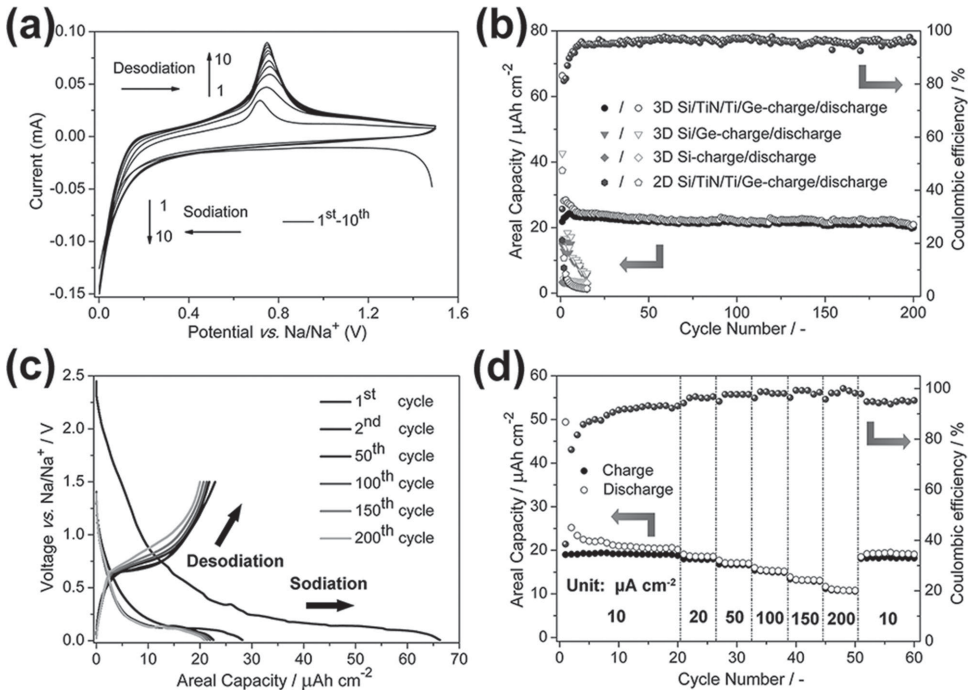

Figure 4. a) The CV measurement of Si/TiN/Ti/Ge composite NR anode at a scan rate of 0.5 mV s^{-1} between 0.001 and 1.5 V versus Na/Na^+ from the 1st to 10th cycle; b) the cycling performances of the 3D Si/TiN/Ti/Ge composite NR anode compared with those in 3D Si/Ge NRs, 3D Si NRs, and planar Si/TiN/Ti/Ge composite as anodes in Na-ion half-cell under a current density of 10 μA cm^{-2} within a voltage window of 0.001–1.5 V versus Na/Na^+; c) the sodiation/desodiation voltage profiles of 3D Si/TiN/Ti/Ge composite NR anodes; d) the rate performances of the 3D Si/TiN/Ti/Ge composite NR anode under different current densities of 10, 20, 50, 100, 150, 200, and 10 μA cm^{-2} between 0.001 and 1.5 V versus Na/Na^+.

poorer cycle performance in the 3D Si/Ge composite NR arrays as the anode in SIBs, it can be indirectly proved that the TiN/Ti layers in the 3D Si/TiN/Ti/Ge composite NR electrode can effectively act as a current collector layer to improve the electronic conductivities and reduce the inner resistance of the whole 3D nanoelectrode. However, the automatic stop of the 3D Si NR anode during the testing process evidences the hardness of Na ions' reversible inserting/deinserting in crystal Si anode materials. Obviously, the amorphous Ge content around the 3D Si/TiN/Ti/Ge composite NR is predominantly responsible for the reversible capacities. In addition, the even poorer charge/discharge performances of the 2D planar Si/TiN/Ti/Ge composite anode for Na half-cell testing further reveals the significance of 3D nanostructure equipped with enough space to accommodate the large volume expansion and larger surface area to promote the Na ion transport during the Na ion ingress/egress process, which are beneficial for the capacity enhancement and stability of the Si/TiN/Ti/Ge composite NR anode. Employing the 3D electrode concept to improve the electrochemical performances of the high-volume-change anode materials can also be found in the LIBs' applications.[23–25] Therefore, both the amorphous Ge sheath layer and the conductive interlayer of TiN/Ti thin film coated on the hexagonal Si NR arrays in a 3D configuration are favorable to improve the electrochemical performances of the corresponding electrodes, which is technically feasible for powering the M/NEMS devices or other smart micro/nanosystems. The excellent cycle performance under higher charge/discharge current densities were also displayed in Figure S2 (Supporting Information).

The sodiation/desodiation voltage profiles of the 3D Si/TiN/Ti/Ge composite NR anode at the 1st, 2nd, 50th, 100th, 150th, and 200th cycle are depicted in Figure 4c. There is an obvious change in the shape of the sodiation (discharge) curves between the 1st and 2nd cycle, which can be ascribed to the irreversible sodiation reaction. Subsequently, all the galvanostatic sodiation/desodiation (discharge/charge) voltage profiles with the consistent voltage platform indicate the stable electrochemical processes as those in the CV measurements shown in Figure 4a. Also, the characteristic of the corresponding

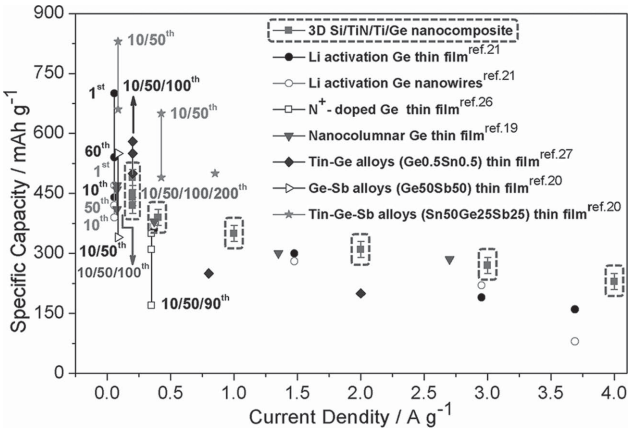

Figure 5. Cycling performance and rate capability for the 3D Si/TiN/Ti/Ge electrode compared with those in previously published Ge-based SIB anodes (The error bar = 20 mAh g^{-1}).[19–21,26,27]

sodiation/disodiation voltage plateaus are almost consistent with the results in other recent works.[19,20] The rate performances of the as-prepared 3D Si/TiN/Ti/Ge composite NR anode were investigated at various current densities and the results are plotted in Figure 4d. After the first 20 cycles at a constant current density of 10 μA cm^{-2}, the current densities of 20, 50, 100, 150, and even up to 200 μA cm^{-2} for every 6 cycles were then imposed and the corresponding areal capacity retention remains at about 90% (19 versus 21 μAh cm^{-2}), 80% (17 versus 21 μAh cm^{-2}), 70% (15 versus 21 μAh cm^{-2}), 60% (13 versus 21 μAh cm^{-2}), and 50% (11 versus 21 μAh cm^{-2}), respectively. The above high capacity retention demonstrates that the sodium ions even with a large radius can diffuse easily and rapidly in the 3D amorphous germanium anode materials. When the current density reduced to the initial value of 10 μA cm^{-2}, the as-prepared 3D Si/TiN/Ti/Ge anode still can resume the areal capacity of 20 μAh cm^{-2}, which once again evidences the stability of this 3D composite electrode during the Na-ions insertion/desertion processes.

Furthermore, compared with previously published results in Ge-based anodes as plotted in **Figure 5** (the specific calculations are illustrated and stated in Figure S3, Supporting Information) and other C-, Sn-, Sb-, and TiO_2-based SIB anodes in Figure S4 (Supporting Information), the specific capacity of the 3D Si/TiN/Ti/Ge NR electrodes fabricated in this work presents the excellent cycle performance maintaining 400 mAh g^{-1} up to the longest cycles of 200 and appreciable rate capability (current density/specific capacity: 0.4/390, 1/350, 2/310, 3/270, 4/230; unit: A g^{-1}/mAh g^{-1}).

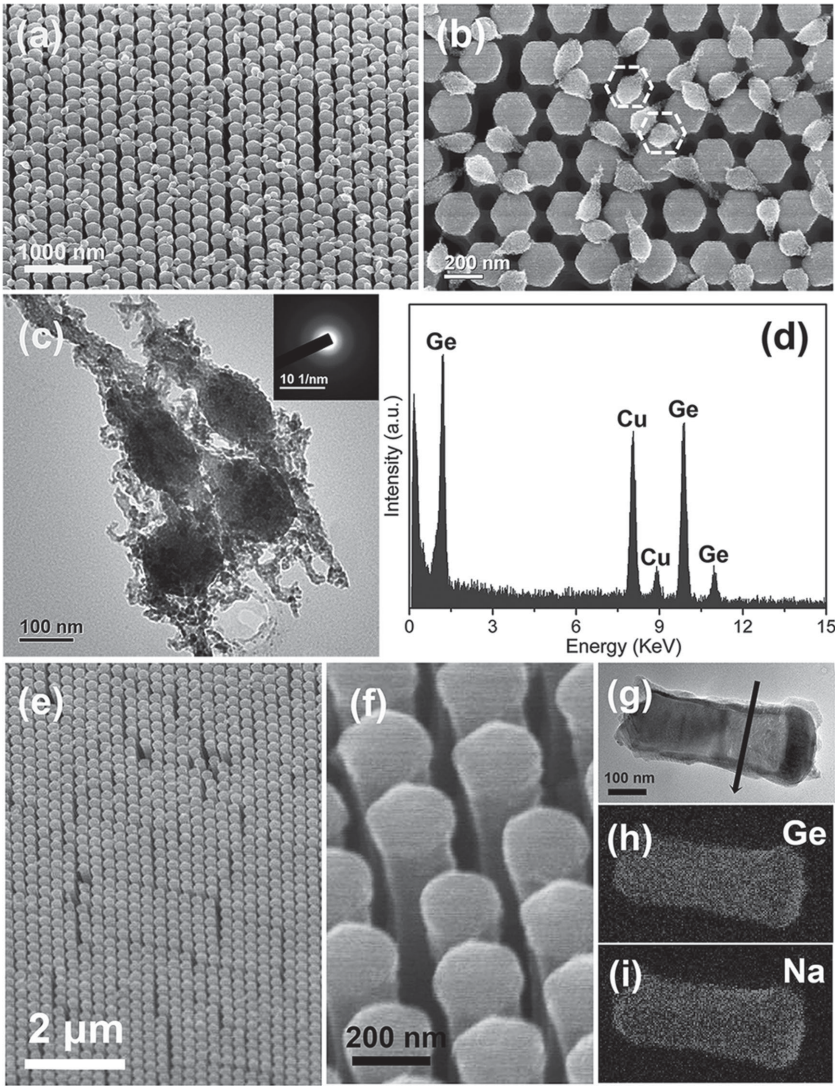

Figure 6. Characterizations of 3D Si/TiN/Ti/Ge composite NR anode after 60 charge/discharge cycles under different current densities: a–b) SEM images of the NR arrays after the cleaning process by DMC, acetone and alcohol; c–d) TEM image of nanoparticles and corresponding EDS pattern taken from the sample (b); e–f) Low and high magnification SEM images of the samples in b) further treated by ultrasonic cleaning in alcohol solution; g) TEM image of an individual composite NR taken from (f) and the corresponding EDS elemental mappings of h) Ge and i) Na.

2.3. Post Morphologies

In order to verify the sodium insertion in 3D Si/TiN/Ti/Ge NR anodes, different washing procedures were developed to wash the cycled anodes and the corresponding postmorphologies of the active material were then characterized by SEM, TEM, and EDS element mappings as shown in **Figures 6** and S5 (Supporting Information). Visually, the different washing procedures, from only acetone wash to DMC–acetone–alcohol-cleaning without or with the followed ultrasonic cleaning in alcoholic solution, can gradually help to eliminate the influences from solid electrolyte interface (SEI) layer and/or remaining electrolyte attached around NRs on the specific characterizations, as seen in Figure S5 (Supporting Information). Apparently, as displayed in Figure 6a,b, after the washing process by DMC, acetone, and alcohol in sequence, the part of Ge sheath, especially in the "match-head" part peeling off from the NR surface might be caused by the remnant electrolyte components and SEI layer removing process. TEM image in Figure 6c and corresponding EDS pattern in Figure 6d further evidence the peeled-off Ge nanoparticles locating at the top part of NR which marked by the hexagonal frame in Figure 6b. After further ultrasonic cleaning process in alcohol, the peeled-off Ge layer was successfully removed so that only thin and close contact Ge film around Si NRs was left, as seen in Figure 6e–f. In this manner, the electrolyte residues and SEI layer can be ignored. Further, the TEM images of an individual cycled Si/TiN/Ti/Ge NR scratched from the sample in Figure 6f and the corresponding EDS element mappings were characterized as displayed in Figure 6g–i. The EDS element mapping patterns as seen in

Figure 6h–i demonstrate that after the above washing process, both the Ge and Na elements exist at the outermost part of the NR surface showing the similar contour in their corresponding EDS elemental mappings. Meanwhile, the other element mappings for the same NR composite are displayed in Figure S6 (Supporting Information). An EDS line scan across the cycled NR surface as marked in Figure 6g also demonstrates the same trend that the Na and Ge elements homogeneously spread in Ge film around the surface of the cycled composite NR, as shown in Figure S7 (Supporting Information). Therefore, based on the above detailed characterizations and analysis to the cycled Si/TiN/Ti/Ge anode materials, the amorphous Ge nanocoatings are mainly responsible for the whole areal capacities due to the formation of Na_xGe alloy during the repeated charge/discharge process. Further work is undergoing to investigate the Na_xGe alloy composition after the Na insertion/extraction process.

2.4. Theoretical Calculation

In order to gain more insights on the preferential inserting ability of the Na ions in Ge anode material over Si, the theoretical investigation employing first principle calculations were performed by the density functional theory (DFT) framework in Vienna ab initio simulation program.[28,29]

The adsorption energy (E_{ad}) of the Na atom on Ge (100) and Si (100) unit cells were calculated from the following definitions

$$E_{ad-Ge(100)} = E_{Na/Ge(100)} - E_{Na} - E_{Ge(100)} \quad (1)$$

$$E_{ad-Si(100)} = E_{Na/Si(100)} - E_{Na} - E_{Si(100)} \quad (2)$$

where $E_{Na/Ge(100)}$ and $E_{Na/Si(100)}$ in Equation (1) and (2) represent the total adsorption energy of one Na atom on a surface position of the Ge (100) and Si (100) unit cells, respectively. The E_{Na}, $E_{Ge(100)}$, and $E_{Si(100)}$ stand for the energies of the individual Na atom, Ge (100), and Si (100) unit cells. The adsorption energies of a single Na atom on the different sites of Ge (100) and Si (100) can be shown in **Figure 7**. Apparently, the adsorption energies of a single Na atom on the Ge (100) and Si (100) structures (2.48 versus 2.91 eV) only have a little difference of about 0.4 eV. However, the subsequent energy barrier of 4.01 eV for Na atom diffusion into the first interstitial site of Ge (100) is much lower than 5.89 eV in the Si unit cell implying the easier Na-ion diffusion in Ge electrodes than in Si anodes, which facilitates the enhancing of the electrochemical performances in Ge composited 3D Si/TiN/Ti NR anode characterized above. Furthermore, the large metastable energy difference between the Ge (100) and Si (100) structures (2.14 versus 3.18 eV) indicates that it is much easier for the Na atom to find a stable site in Ge lattice than in Si. Therefore, the lower diffusion energy of Na in Ge structure compared with that in Si is the fundamental origin for improving the electrochemical kinetics in Ge-composited anodes applied in SIBs.

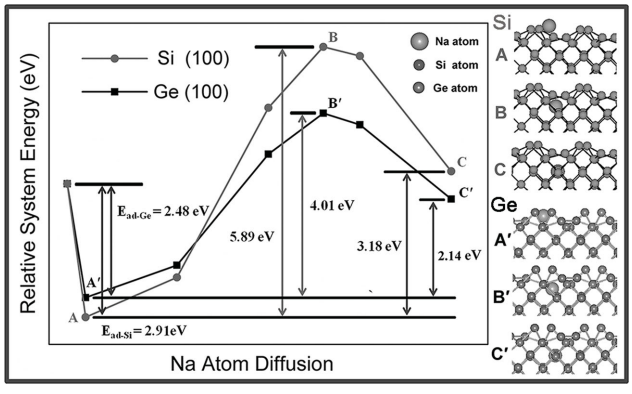

Figure 7. Graphical plot of the relative system energies of the Na adsorption and diffusion in the Ge (100) structure with a comparison to the Si (100) structure.

3. Conclusion

In summary, the unique amorphous Ge anode material coated on the 3D hexagonal Si NR arrays using the TiN/Ti interlayer as the current collector for rechargeable sodium-ion micro/nanobatteries embraces an improved electrochemical performance compared with the only Si/Ge, Si 3D nanostructures and other reported SIB anodes. The amorphous Ge electrode material in the 3D configuration and the effective TiN/Ti electron conductive layer are believed to be responsible for the excellent cycling stability maintained in the Si/TiN/Ti/Ge nanocomposite electrodes. Detailed postmorphology characterizations performed in the cycled composite NRs anode further verified the preferential Na^+ insertion in Ge-active material. More significantly, with the comparison to Si, the lower Na diffusion energy in Ge unit cell calculated by the first principles ab initio method reveals the mechanism to the enhanced electrochemical properties in the Ge-composited 3D Si/TiN/Ti NR anode. Therefore, this work provides a promising way to fabricate the optimized 3D SIBs, which can be potentially integrated with the micro/nanosemiconductor devices in the future.

Supporting Information

Supporting Information is available from the Wiley Online Library or from the author.

Acknowledgements

This work is financially supported by the National Natural Science Foundation of China (Grant No. 61106118,61227009,91321102 and U1405253), Science and Technology Project of Fujian Province of China (Grant No. 2013H0046), Fundamental Research Funds for the Central Universities, and the China Scholarship Council (CSC) scholarship under the State Scholarship Fund.

Received: October 19, 2014
Revised: December 19, 2014
Published online: January 14, 2015

[1] S. Thompson, S. Parthasarathy, *Mater. Today* **2006**, *9*, 20.
[2] Y. H. Liu, Y. He, M. Li, *IEEE Trans. Parallel Distributed Syst.* **2013**, *24*, 1983.

[3] J. W. Long, B. Dunn, D. R. Rolison, H. S. White, *Chem. Rev.* **2004**, *104*, 4463.
[4] T. S. Arthur, D. J. Bates, N. Cirigliano, D. C. Johnson, P. Malati, J. M. Mosby, E. Perre, M. T. Rawls, A. L. Prieto, B. Dunn, *MRS Bull.* **2011**, *36*, 523.
[5] M. Erol-Kantarci, H. T. Mouftah, *IEEE Wireless Commun. 19*, **2012**, 30.
[6] J. Jeong, D. Culler, *ACM Trans. Sens. Netw.* **2012**, *9*, 1.
[7] L. Baggetto, H. C. M. Knoops, R. A. H. Niessen, W. M. M. Kessels, P. H. L. Notten, *J. Mater. Chem.* **2010**, *20*, 3703.
[8] A. Kohandehghan, P. Kalisvaart, K. Cui, M. Kupsta, E. Memarzadeha, D. Mitlin, *J. Mater. Chem. A* **2013**, *1*, 12850.
[9] P. H. L. Notten, F. Roozeboom, R. A. H. Niessen, L. Baggetto, *Adv. Mater.* **2007**, *19*, 4564.
[10] M. D. Slater, D. Kim, E. Lee, C. S. Johnson, *Adv. Funct. Mater.* **2013**, *23*, 947.
[11] V. Palomares, P. Serras, I. Villaluenga, K. B. Hueso, J. C. González, T. Rojo, *Energy Environ. Sci.* **2012**, *5*, 5884.
[12] B. Dunn, H. Kamath, J. M. Tarascon, *Science* **2011**, *334*, 928.
[13] J. W. Wang, X. H. Liu, S. X. Mao, J. Y. Huang, *Nano Lett.* **2012**, *12*, 5897.
[14] A. Darwiche, C. Marino, M. T. Sougrati, B. Fraisse, L. Stievano, L. Monconduit, *J. Am. Chem. Soc.* **2012**, *134*, 20805.
[15] S. Komaba, W. Murata, T. Ishikawa, N. Yabuuchi, T. Ozeki, T. Nakayama, A. Ogata, K. Gotoh, K. Fujiwara, *Adv. Funct. Mater.* **2011**, *21*, 3859.
[16] S. W. Kim, D. H. Seo, X. H. Ma, G. Ceder, K. Kang, *Adv. Energy Mater.* **2012**, *2*, 710.
[17] J. F. Qian, M. Zhou, Y. l. Cao, X. P. Ai, H. X. Yang, *Adv. Energy Mater.* **2012**, *2*, 410.
[18] V. L. Chevrier, G. Ceder, *J. Electrochem. Soc.* **2011**, *158*, 1011.
[19] P. R. Abel, Y. M. Lin, T. Souza, C. Y. Chou, A. Gupta, J. B. Goodenough, G. S. Hwang, A. Heller, C. B. Mullins, *J. Phys. Chem. C* **2013**, *117*, 18885.
[20] B. Farbod, K. Cui, W. P. Kalisvaart, M. Kupsta, B. Zahiri, A. Kohandehghan, E. M. Lotfabad, Z. Li, E. J. Luber, D. Mitlin, *ACS Nano* **2014**, *8*, 4415.
[21] A. Kohandehghan, K. Cui, M. Kupsta, J. Ding, E. M. Lotfabad, W. P. Kalisvaart, D. Mitlin, *Nano Lett.* **2014**, *14*, 5872.
[22] P. R. Abel, A. M. Chockla, Y. M. Lin, V. C. Holmberg, J. T. Harris, B. A. Korgel, A. Heller, C. B. Mullins, *ACS Nano* **2013**, *7*, 2249.
[23] X. F. Li, A. Dhanabalan, L. Gu, C. L. Wang, *Adv. Energy Mater.* **2012**, *2*, 238.
[24] X. F. Li, X. B. Meng, J. Liu, D. S. Geng, Y. Zhang, M. N. Banis, Y. L. Li, J. L. Yang, R. Y. Li, X. L. Sun, M. Cai, M. W. Verbrugge, *Adv. Funct. Mater.* **2012**, *22*, 1647.
[25] X. F. Li, C. L. Wang, *J. Mater. Chem. A* **2013**, *1*, 165.
[26] L. Baggetto, J. K. Keum, J. F. Browning, G. M. Veith, *Electrochem. Commun.* **2013**, *34*, 41.
[27] P. R. Abel, M. G. Fields, A. Heller, C. Buddie, *ACS Appl. Mater. Interfaces* **2014**, *6*, 15860.
[28] Kresse, G. Furthmüller, *Phys. Rev. B* **1996**, *54*, 11169.
[29] Y. J. Yu, C. Yue, S. B. Sun, W. Lin, H. Su, B. B. Xu, J. T. Li, S. T. Wu, J. Li, J. Y. Kang, *ACS Appl. Mater. Interfaces* **2014**, *6*, 5884.